PROBING THE MASS-LOSS HISTORY OF THE YELLOW HYPERGIANT IRC+10420

Dinh-V-Trung[1,4], Sébastien Muller[1], Jeremy Lim[1], Sun Kwok[2], and C. Muthu[3]

[1] Institute of Astronomy and Astrophysics, Academia Sinica, P.O. Box 23-141, Taipei 106, Taiwan; trung@asiaa.sinica.edu.tw, muller@asiaa.sinica.edu.tw, jlim@asiaa.sinica.edu.tw

[2] Department of Physics, Faculty of Science, University of Hong Kong, Hong Kong; sunkwok@hku.hk

[3] Vainu Bappu Observatory, Indian Institute of Astrophysics, Kavalur, 635 701, India; muthu@iiap.res.in

ABSTRACT

We have used the submillimeter array to image the molecular envelope around the yellow hypergiant IRC+10420. Our observations reveal a large and clumpy expanding envelope around the star. The molecular envelope shows a clear asymmetry in ^{12}CO $J = 2$–1 emission in the southwest direction. The elongation of the envelope is found even more pronounced in the emission of ^{13}CO $J = 2$–1 and SO $J_K = 6_5$–5_4. A small positional velocity gradient across velocity channels is seen in these lines, suggesting the presence of a weak bipolar outflow in the envelope of IRC+10420. In the higher resolution ^{12}CO $J = 2$–1 map, we find that the envelope has two components: (1) an inner shell (shell I) located between radius of about $1''$ and $2''$; (2) an outer shell (shell II) located between $3''$ and $6''$ in radius. These shells represent two previous mass-loss episodes from IRC+10420. We attempt to derive in self-consistent manner the physical conditions inside the envelope by modeling the dust properties, and the heating and cooling of molecular gas. We estimate a mass-loss rate of $\sim 9 \times 10^{-4}$ $M_\odot$ yr^{-1} for shell I and 7×10^{-4} $M_\odot$ yr^{-1} for shell II. The gas temperature is found to be unusually high in IRC+10420 in comparison with other oxygen-rich envelopes. The elevated gas temperature is mainly due to higher heating rate, which results from the large luminosity of the central star. We also derive an isotopic ratio $^{12}C/^{13}C = 6$.

Key words: circumstellar matter – ISM: molecules – stars: AGB and post-AGB – stars: individual (IRC+10420) – stars: mass loss

Online-only material: color figures

1. INTRODUCTION

Yellow hypergiants are rare objects which are post-red supergiants rapidly evolving in blueward loops in the Hertzsprung–Russell diagram (de Jager 1998). A few of such objects are found to have prodigious mass loss, leading to the formation of thick circumstellar envelopes. The study of the circumstellar envelope around them is very important to provide insight into the mass-loss process from these massive stars and the evolution of stars themselves.

The star IRC+10420 is classified as yellow hypergiant (de Jager 1998). Based on spectroscopic monitoring, the star initially classified as spectral type F8 I_a^+ in 1973 (Humphreys et al. 1973) has evolved into spectral type A in 1990 (Oudmaijer et al. 1996; Klochkova et al. 1997). Strong emission lines such as the Balmer series and Ca II triplets are seen in its optical spectrum (Oudmaijer 1998). Broad wings seen in Hα and Ca II triplets suggest a large outflow velocity in a massive wind close to the stellar surface. High-resolution optical images of IRC+10420 (Humphreys et al. 1997) revealed a complex circumstellar environment with many features such as knots, arcs, or loops. Lacking kinematic information, however, the real three-dimensional structure of the envelope cannot be inferred. Recently, through integral-field spectroscopy of Hα emission line, Davies et al. (2007) show strong evidence for axisymmetry in the circumstellar envelope.

The molecular envelope around IRC+10420 is very massive and is a rich source of molecular lines (Quintana-Lacaci et al. 2007). The mass-loss rate estimated from CO observations is

at the upper end seen toward evolved stars, up to a few times 10^{-4} $M_\odot$ yr^{-1} (Knapp & Morris 1985; Oudmaijer et al. 1996). High-density tracers such as ammonia (NH$_3$) and HCN lines have been detected (Menten & Alcolea 1995). Molecules typical of oxygen-rich envelope such as SO and SO$_2$ (Sahai & Wannier 1992; Omont et al. 1993) are known to be present. IRC+10420 is also a strong OH maser source, exhibiting both the main lines (1665 MHz and 1667 MHz) maser and the satellite line (1612 MHz) maser. By comparison with typical OH/IR stars, IRC+10420 has the warmest envelope harboring OH masers (Humphreys et al. 1997). High angular resolution imaging of the OH masers by Nedoluha & Bowers (1992) shows that the maser emissions are distributed in an oblate expanding shell measuring $1''.5$ in radius. Recently, Castro-Carrizo et al. (2007) presented high angular resolution ($\sim 3''$ and $1''.4$) mapping of the envelope around IRC+10420 in ^{12}CO $J = 1$–0 and $J = 2$–1 lines. Their observations reveal an expanding but complex molecular envelope with an inner cavity around the central star, implying a recent dramatic decrease in the mass loss from IRC+10420. In addition, the shell shows some elongation in the northeast to southwest direction, suggesting a nonspherical symmetry in the mass-loss process. From excitation analysis of ^{12}CO lines, Castro-Carrizo et al. (2007) show the presence of two separate shells with mass loss in the range 1.2×10^{-4} to 3×10^{-4} $M_\odot$ yr^{-1}. Interestingly, the gas temperature in shells derived from their model fitting is unusually high, 100 K even at the large radial distance of $\sim 2 \times 10^{17}$ cm.

The distance to IRC+10420 is still uncertain. From analysis of photometric and polarimetric data, Jones et al. (1993) conclude that IRC+10420 is located at a large distance, between 4 and 6 kpc. Here we adopt a distance to IRC+10420 of 5 kpc, similar to that adopted in Castro-Carrizo et al. (2007).

---

[4] On leave from Center for Quantum Electronics, Institute of Physics, Vietnamese Academy of Science and Technology, 10 DaoTan, ThuLe, BaDinh, Hanoi, Vietnam.

Table 1
Basic Data of IRC+10420 and Its Molecular Envelope

Parameter	Value	Reference
R.A. (J2000)	$19^h26^m48\overset{s}{.}03$	(1)
Decl. (J2000)	$11°21'16\overset{''}{.}7$	(1)
Distance	5 kpc	(2)
Angular scale	$1'' \sim 5000\ AU \sim 7.5 \times 10^{16}\ cm$	
Luminosity, L_*	$\sim 6 \times 10^5\ L_\odot$	(2)
Spectral type	mid-A type	(3,4)
Effective temperature, T_{eff}	7000 K	(3)
Stellar radius	1.66 AU	
Systemic velocity	$V_{LSR} = 74\ km\ s^{-1}$	(3)
Expansion velocity	$V_{exp} = 40\ km\ s^{-1}$	(3)
Mass-loss rate, $\dot{M}$	$\sim 6.5 \times 10^{-4}\ M_\odot\ yr^{-1}$	(5)

References. (1) SIMBAD database; (2) Jones et al. (1993); (3) Oudmaijer et al. (1996); (4) Klochkova et al. (1997); (5) Knapp & Morris (1985).

In this paper, we present high angular resolution observations of the molecular envelope around IRC+10420. We also perform detailed modeling to derive in a self-consistent manner the dust properties and molecular gas temperature profile in the envelope.

2. OBSERVATIONS

We have observed IRC+10420 in the 1.3 mm band with the submillimeter array (SMA) at two different epochs and in two different configurations as summarized in Table 2. The first observation was carried out on 2004 June 21, with eight antennas in an extended configuration, giving projected baselines from 27 to 226 m. The weather was good during the observation with zenith atmospheric opacity of $\tau_{225\ GHz} \sim 0.2$ at 225 GHz and the system temperatures ranged between 200 and 600 K. The second observation was carried on 2005 July 2, with seven antennas in a compact configuration, giving projected baselines in the range from 11 to 69 m. The weather was very good with $\tau_{225\ GHz} \sim 0.1$ and the system temperatures ranged between 100 and 200 K.

In each observation, the correlator of the SMA was configured in the normal mode with two 2 GHz bandwidth windows separated by 10 GHz. This allowed us to cover simultaneously the $^{12}CO\ J = 2–1$ line in the upper sideband (USB) the ^{13}CO $J = 2–1$ and SO $6_5–5_4$ lines in the lower sideband (LSB). The bandpass of individual antennas was calibrated using the quasar 0423-013 for the observation taken in 2004 and Uranus for observation taken in 2005. To improve the signal-to-noise ratio of the data, we smoothed data from the instrumental spectral resolution of 0.8125–3.25 MHz (i.e., $\sim$4 km s^{-1}). For comparison, the observed lines have velocity widths of $\sim$80 km s^{-1}. The nearby quasars 1751+096 and 1925+211 were observed at regular intervals to correct for gain variations of the antennas due to atmospheric fluctuations. The data reduction

and calibration were done under MIR/IDL.[5] After the gain and bandpass calibrations, the visibilities data from both tracks were combined together. Imaging and deconvolution were performed under GILDAS[6] package.

The 1.3 mm (225 GHz) continuum emission map (see Figure 1) was derived by averaging the line-free channels from both LSB and USB, resulting in a total bandwidth of 3.4 GHz. For the line channel maps, we subtract the continuum visibilities of the relevant sideband from the line emission visibilities. In Table 2, we summarize the observations of IRC+10420 carried out by the SMA.

For the sake of presentation clarity, the center of all the maps were shifted in the visibility domain so that the phase reference matches the position of the continuum peak emission, i.e., R.A. = $19^h26^m48\overset{s}{.}09$ and decl. = $11°21'16\overset{''}{.}75$, which also corresponds to the center of the SiO shell detected by Castro-Carrizo et al. (2001). We note that the lack of interferometric baselines shorter than 11 m makes our observations blind to extended structures of size $\geqslant 25''$. In order to estimate the amount of flux recovered by the SMA, we convolved the channel maps of $^{12}CO\ J = 2–1$ and $^{13}CO\ J = 2–1$ lines to the spatial resolution of $19\overset{''}{.}7$ and $12''$, respectively. We show in Figure 2 the spectra taken from these maps and the single dish observations taken by Kemper et al. (2003) and Bujarrabal et al. (2001) at the same angular resolutions. We estimate that the SMA recovered more than 60% of the flux in $^{12}CO\ J = 2–1$ line and almost all the flux in $^{13}CO\ J = 2–1$ line.

3. RESULTS

3.1. 1.3 mm Continuum Emission

As shown in Figure 1, the 1.3 mm continuum emission from IRC+10420 was well detected in our SMA data. The emission is not resolved and has a flux density $\sim$45 mJy. A previous single-dish observation by Walmsley et al. (1991) also at 1.3 mm gives a flux of 101 mJy. That suggests that the dust emission is extended, with about 55% of the continuum flux resolved out by the interferometer. Assuming the central star to have a black body spectrum with a temperature of $T_{eff} = 7000$ K, it contributes only a negligible amount of the flux at 1.3 mm of $S_* \sim 0.1$ mJy. Thus, most of the 1.3 mm continuum emission is produced by the warm dust in the envelope around IRC+10420.

3.2. $^{12}CO\ J = 2–1$ Emission

In Figure 3, we show the channel maps of the $^{12}CO\ J = 2–1$ emission obtained with the compact configuration of the SMA. At our angular resolution of $\sim$3$''$, the envelope is well resolved. At both blueshifted and redshifted velocities the emission appears to be circularly symmetric, as is expected for a spherically expanding envelope. More interestingly, at velocities

---

[5] http://cfa-www.harvard.edu/~cqi/mircook.html
[6] http://www.iram.fr/IRAMFR/GILDAS/

Table 2
SMA Line Observations Toward IRC+10420

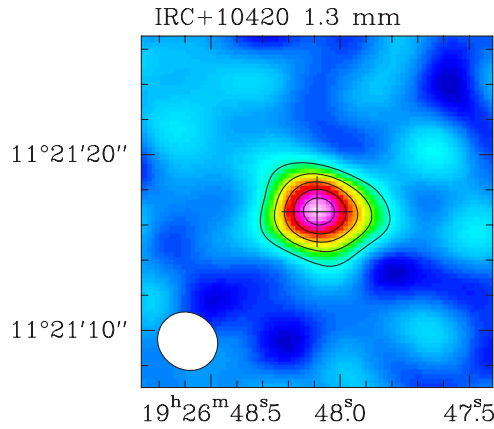| Line	Rest Freq. (GHz)	Config.	Clean Beam (FWHM, arcsec)	PA (deg)	ΔV (km s^{-1})	1σ rms (mJy beam^{-1})
$^{12}CO(2–1)$	230.538	Comp	3.44×3.12	46	4.2	60
		Comp+Ext	1.44×1.12	46	4.2	80
$^{13}CO(2–1)$	220.399	Comp	3.52×3.21	63	4.4	50
$SO(6_5–5_4)$	219.949	Comp	3.51×3.19	63	4.4	50

Figure 1. 1.3 mm continuum emission map of IRC+10420 obtained with the SMA compact configuration. The synthesized beam is $3''.52 \times 3''.21$ (PA = 54°) as indicated by the ellipse in the bottom left corner. Contour levels are every 6 mJy beam^{-1} ($\sim 3\sigma$).

(A color version of this figure is available in the online journal.)

Figure 2. Spectra of ^{12}CO $J = 2$–1 (top), ^{13}CO $J = 2$–1 (middle), and SO(6_5–5_4) (bottom) transitions toward IRC+10420. The spectra are shown in main beam brightness temperature with a telescope beam as mentioned in the top right corner of each box. The dotted lines show the spectra of ^{12}CO $J = 2$–1 obtained with JCMT (Kemper et al. 2003) and ^{13}CO $J = 2$–1 obtained with the IRAM 30 m (Bujarrabal et al. 2001)

between 59 and 89 km s^{-1}, centered around the systemic velocity, the envelope is clearly elongated in approximately the northeast to southwest direction. By fitting a two-dimensional Gaussian to the intensity distribution of the ^{12}CO $J = 2$–1 emission at systemic velocity $V_{\rm LSR} = 74$ km s^{-1}, we obtain a position angle for the ^{12}CO $J = 2$–1 envelope of PA = 70°. The orientation of the CO emission is consistent with the elongation found by Castro-Carrizo et al. (2007). The position–velocity (PV) diagrams of the ^{12}CO $J = 2$–1 emission along the major (PA $\sim$70°) and minor (PA $\sim$ 160°) axes of the envelope as presented in Figure 7 are typical of an expanding envelope at an expansion velocity of $\sim$40 km s^{-1}.

We show in Figure 4 the channel maps of the ^{12}CO $J = 2$–1 emission, which is obtained by combining the data from both compact and extended configurations of the SMA. The ^{12}CO $J = 2$–1 emission is further resolved into more complex structures. In the velocity channels between 59 and 89 km s^{-1}, centered around the systemic velocity, the ^{12}CO $J = 2$–1 emission consists of a central prominent hollow shell structure of $\sim$1″–2″ in radius and a more clumpy arc or shell located between radii of 3″ and 6″, which is more prominent in the southwest quadrant of the envelope. Close inspection of the velocity channels around the systemic velocity $V_{\rm LSR} \sim 74$ km s^{-1} indicates that the central hollow shell-like structure is clumpy and shows stronger emission toward the southwestern side. The outer arc or shell of emission can be seen more easily in the azimuthal average of the ^{12}CO $J = 2$–1 brightness temperature as shown in Figure 13. We can clearly see a central depression within a radius of $\sim$1″ and enhanced emission between the radii of 3″ and 6″.

3.3. ^{13}CO $J = 2$–1 Emission

The channel maps of ^{13}CO $J = 2$–1 emission obtained from the compact configuration data at an angular resolution of $\sim$3″5 are shown in Figure 5. The emission in the ^{13}CO $J = 2$–1 line appears fainter and more compact then seen in the main isotope ^{12}CO $J = 2$–1 line. Like in ^{12}CO $J = 2$–1 emission, near the systemic velocity, the envelope traced by ^{13}CO $J = 2$–1 emission is elongated at position angle of PA $\sim$ 70°. The centroid of the emission appears to be slightly offset from the stellar position. Also like in ^{12}CO $J = 2$–1 emission, at higher velocities in both blue-shifted and redshifted parts the ^{13}CO
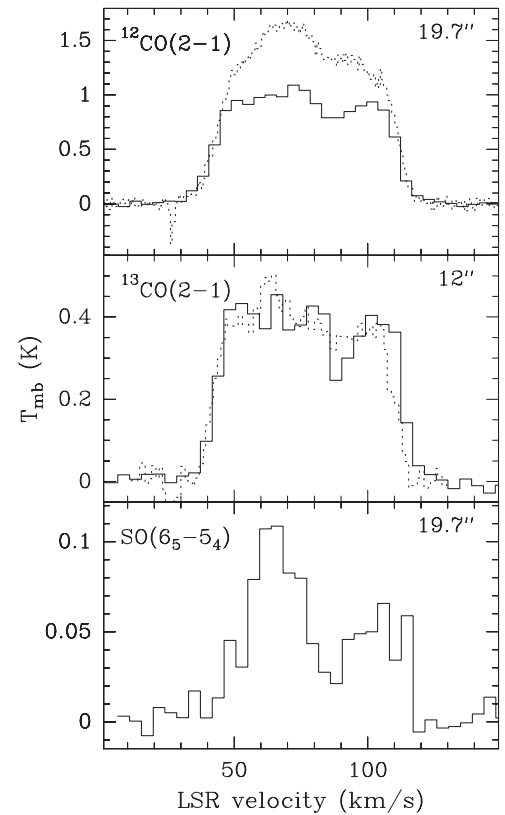
$J = 2$–1 emission again shows a roughly circularly symmetric morphology, as would be expected for a spherically expanding envelope. The spatial kinematics of the ^{13}CO $J = 2$–1 emission can be more clearly seen in the PV diagram (Figure 7) along the major axis (PA $\sim$ 70°) of the envelope. In the PV diagram, there is a small velocity gradient in the velocity range between 70 and 100 km s^{-1}. Closer inspection of the channel maps suggests that the small velocity gradient corresponds to the slight shift of the emission centroid toward the northeast quadrant of the envelope in the above-mentioned velocity range.

3.4. SO $J_{\rm K} = 6_5$–5_4 Emission

In Figure 6, we show channel maps of the SO 6_5–5_4 emission obtained from the data of the compact configuration. The emission is well resolved in some of the velocity channels. A close inspection reveals that the distribution of SO 6_5–5_4 emission is different from that of ^{12}CO $J = 2$–1. At extreme redshifted velocities, the centroid of the emission is shifted to the east, whereas at extreme blueshifted velocities the centroid of the emission is shifted to the west. In addition, the SO 6_5–5_4 emission in velocity channels centered around the systemic velocity is clearly elongated to the southwest. This elongation is very similar to that seen in ^{12}CO $J = 2$–1 emission at the same angular resolution (see Figure 3). More interestingly, at the opposing redshifted velocities of 84–102 km s^{-1} (see Figure 6) the emission is very compact and shifts to the northeast of the central star. Such positional shift is shown more clearly in the PV diagram of the SO $J_K = 6_5$–5_4 emission along the major

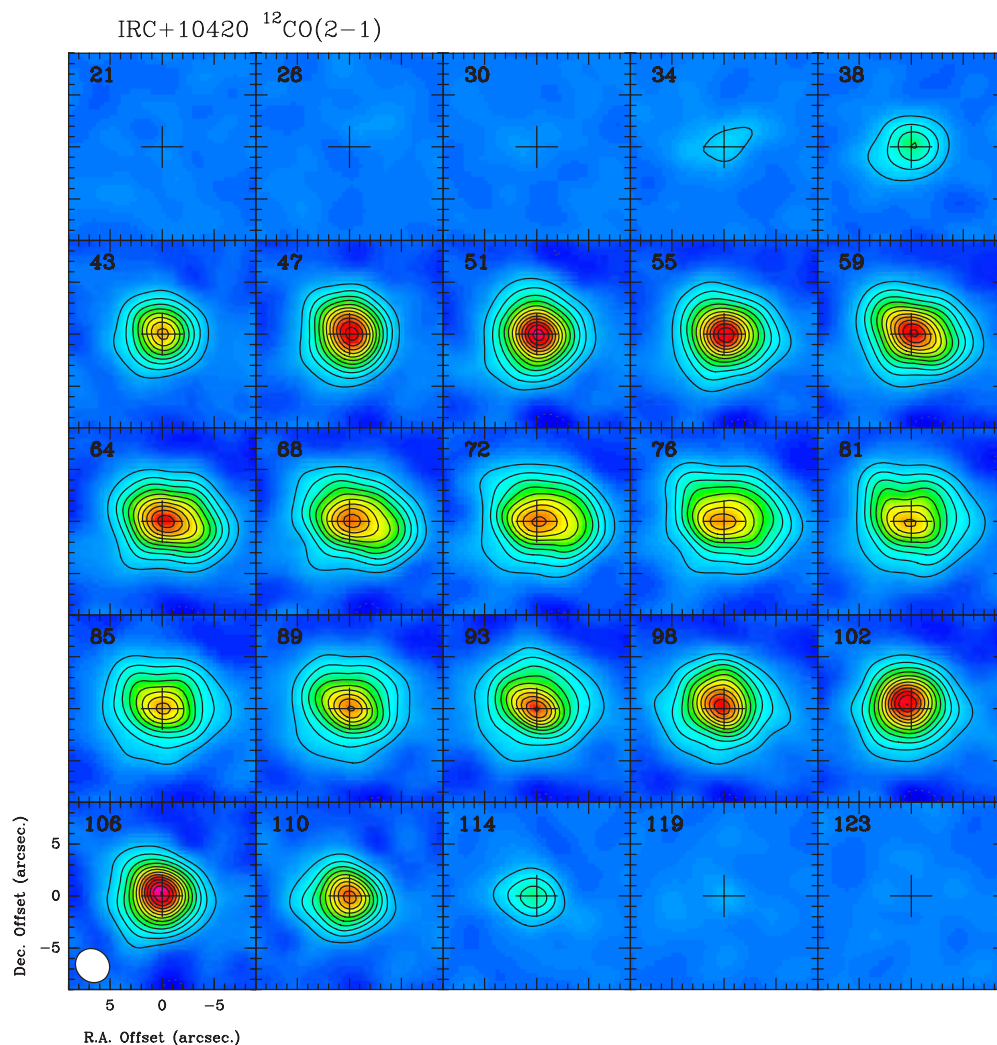**Figure 3.** Channel maps of the ^{12}CO $J = 2$–1 line emission obtained from the SMA compact configuration alone. The synthesized beam is $3''.44 \times 3''.12$ (PA $= 46°$) and is indicated in the bottom left corner of the figure. Contour levels are drawn every 0.6 Jy beam^{-1} or 1.3 K ($\sim 10\sigma$). The velocity resolution is 4.2 km s^{-1}. The cross indicates the position of the continuum peak emission.

(A color version of this figure is available in the online journal.)

axis (PA $\sim 70°$) of the envelope (see Figure 7). There is a clear velocity gradient in the velocity range between 70 and 90 km s^{-1}, which is similar but more pronounced that that seen in ^{13}CO $J = 2$–1 line.

Thus, the SO 6_5–5_4 emission in particular but also the ^{13}CO $J = 2$–1 emission seem to better trace the asymmetric structure inside the envelope. The small velocity gradient seen in both lines points to the presence of an ejecta in the envelope of IRC+10420. From the above-mentioned elongation of the envelope and the orientation of the positional velocity shift, we estimate that the ejecta is oriented at position angle of PA $= 70°$. We note that SO emission is known to be enhanced in asymptotic giant branch (AGB) and post-AGB envelopes where collimated high velocity outflows are present. Examples can be found in the rotten egg nebula OH 231.8+4.2 (Sánchez Contreras et al. 2000) and VY CMa (Muller et al. 2007). In both cases, SO emission is found to be strongly enhanced in the bipolar lobes. The SO enhancement in bipolar outflows could be related to the synthesis of SO in the shocked molecular gas in these outflows. Alternatively, the warm environment around supergiants such as VY CMa and IRC+10420 could facilitate the synthesis of SO

through chemical pathways such as S + OH $\longrightarrow$ SO + H or HS + O $\longrightarrow$ SO + H (Willacy & Millar 1997).

4. STRUCTURE OF THE ENVELOPE

In this section, we attempt to build a model for the circumstellar envelope of IRC+10420 using our newly obtained SMA data and also the large body of observational data on IRC+10420, ranging from optical to millimeter wavelengths. Our goal is to better understand the physical conditions of the molecular gas inside the envelope and also to retrace the mass-loss history of the central star. The structure of the envelope around IRC+10420 has been previously modeled in the work of Castro-Carrizo et al. (2007), by prescribing a radial distribution for the temperature in order to derive the gas density and consequently the mass-loss rate. In our model, we take into account the properties of the dust inside envelope and the balance of heating and cooling processes. From the discussion in the previous section, the envelope can be approximated as spherically symmetric. The physical conditions such as kinetic temperature, density in the envelope can then be inferred from detailed
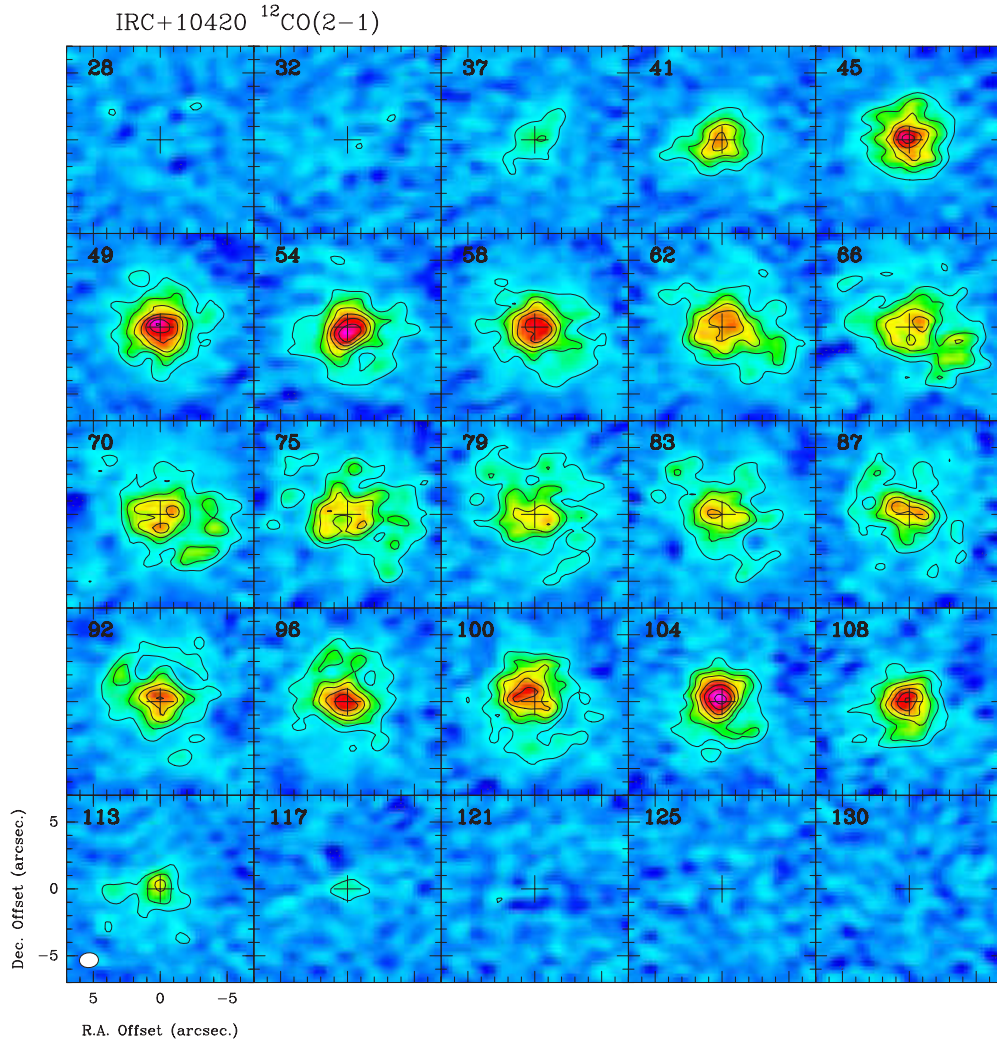
IRC+10420 ^{12}CO(2−1)

Figure 4. Channel maps of the ^{12}CO $J = 2$–1 line emission obtained by combining data from compact and extended configurations. The synthesized beam is $1''.44 \times 1''.12$ (PA = 46°) and is indicated in the bottom left corner of the figure. Contour levels are drawn every 0.24 Jy beam^{-1} or 3.4 K ($\sim 3\sigma$). The velocity resolution is 4.2 km s^{-1}. The cross indicates the position of the continuum peak emission.

(A color version of this figure is available in the online journal.)

calculations of the energy balance within the envelope and matching the predictions of the radiative transfer model to the observed strength of the CO rotational lines. This procedure represents an improvement in comparison to previous models, and allows a better understanding of the physical conditions in the envelope of IRC+10420.

4.1. A Simple Model for Dust Continuum Emission

To determine the heating process in the detected molecular shells requires knowledge of the momentum transfer coefficient (or the flux-averaged extinction coefficient $\langle Q \rangle$) between the dust particles and the gas molecules. To estimate this quantity, we follow the treatment of Oudmaijer et al. (1996) who modeled in detail the spectral energy distribution (SED) of IRC+10420. We emphasize here that by following the treatment of Oudmaijer et al. (1996) the structure of the molecular envelope as seen in our SMA data and previously in the data of Castro-Carrizo et al. (2007) is not considered explicitly.

We use the photometric data of IRC+10420 collected by Jones et al. (1993) and Oudmaijer et al. (1996), i.e., the 1992 photometric data set. We also assume that the dust consists of silicate particles with a radius of $a = 0.05\ \mu$m. The dust opacity

as a function of wavelength is taken from the work of Volk & Kwok (1988). Following Oudmaijer et al. (1996), we scale the opacity law to match the absolute value of the opacity at 60 μm of $\kappa_{60\ \mu m} = 150$ cm^2 g^{-1}. We also a use a specific density for dust particles of $\rho = 2$ g cm^{-3} and assume a dust to gas ratio $\Psi = 5 \times 10^{-3}$ as used by Oudmaijer et al. (1996).

To fit the SED of IRC+10420, especially in the mid-IR region between 5 and 20 μm, Oudmaijer et al. (1996) suggest that two dust shells are needed: a hot inner shell with a low mass-loss rate and an outer cooler shell with a higher mass-loss rate. We note that Blöcker et al. (1999) also reached the same conclusion in their attempt to fit the SED of IRC+10420. In our model, we also use two dust shells: a hot inner shell with a low mass-loss rate of $\dot{M} = 8 \times 10^{-5}\ M_{\odot}$ yr^{-1} located between 2.6×10^{15} cm (70 stellar radii) and 1.8×10^{16} cm (486 stellar radii) and an outer cooler shell with a higher mass-loss rate of $\dot{M} = 1.2 \times 10^{-3}\ M_{\odot}$ yr^{-1} extending to a radial distance of 10^{18} cm where the dust particle number density drops to very low values. We also infer a stellar luminosity of $6 \times 10^5\ L_{\odot}$. The size of the dust shells, the mass-loss rates, and the stellar luminosity are very similar to that derived by Oudmaijer et al. (1996) scaled to the adopted distance of 5 kpc. The results of our radiative transfer model
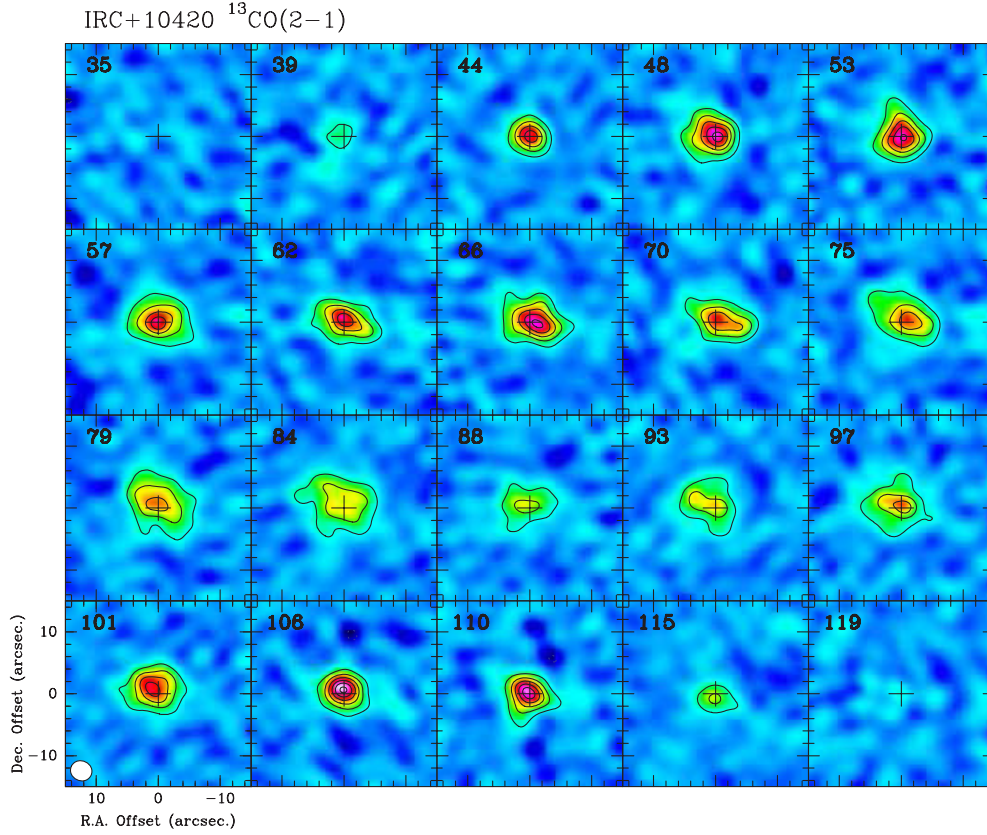
IRC+10420 ^{13}CO(2−1)

Figure 5. Channel maps of the ^{13}CO $J = 2-1$ line emission obtained from the SMA compact configuration alone. The synthesized beam is $3''.52 \times 3''.21$ (PA $= 63°$) and is indicated in the bottom left corner of the figure. Contour levels are drawn every 0.2 Jy beam^{-1} or 0.45 K ($\sim 4\sigma$). The velocity resolution is 4.4 km s^{-1}. The cross indicates the position of the continuum peak emission.

(A color version of this figure is available in the online journal.)

are presented in Figures 8 and 9. The fluxes from the model are corrected for an interstellar extinction of $A_V = 5$ as suggested by Oudmaijer et al. (1996). As can be seen in Figure 8, the results of our model are in close agreement with that shown in Oudmaijer et al. (1996) and match reasonably the observed SED of IRC+10420. As shown in Figure 9, the dust temperature decreases monotonically from ~ 1000 K at the inner radius to ~ 50 K at the outer radius of the dust envelope, even though there is a jump in mass-loss rate between the inner hot dust shell and the outer cooler dust shell at a radial distance of 1.8×10^{16} cm.

From the flux F_λ of the radiation field at each point in the envelope we can define the flux-averaged extinction coefficient $\langle Q \rangle$, which characterizes the transfer of angular momentum from radiation photons to dust particles during the absorption and reemission processes of the continuum radiation. Because in our case we do not consider the scattering of radiation, the extinction coefficient Q_λ is simply the opacity κ_λ, where λ is the wavelength of the radiation,

$$\langle Q \rangle = \frac{\int_0^\infty F_\lambda Q_\lambda d\lambda}{\int_0^\infty F_\lambda d\lambda} = \frac{\int_0^\infty F_\lambda \kappa_\lambda d\lambda}{\int_0^\infty F_\lambda d\lambda}. \quad (1)$$

The flux-averaged extinction coefficient $\langle Q \rangle$ changes significantly in the inner part of the dust envelope but reaches a constant value in the outer part. Because the molecular shells are located in the outer part of the dust envelope, at radii larger than a few times 10^{16} cm; for simplicity, we will adopt a constant value $\langle Q \rangle = 0.025$ (see Figure 9).

4.2. Excitation of CO Molecule

The temperature of the molecular gas at any point in the envelope is determined by the balance between cooling due to adiabatic expansion and molecular emissions, and the heating, which is mainly due to collisions of molecules with dust grains (Goldreich & Scoville 1976). As the dust grains stream through the gas under radiation pressure, the grains transfer angular momentum to the gas by collisions. The heating term is therefore directly related to the drift velocity:

$$H = \tfrac{1}{2}\rho\pi a^2 n_d v_{\mathrm{drift}}^3, \quad (2)$$

where n_d is the number density of dust particles. The drift velocity is determined by the relation

$$v_{\mathrm{drift}} = \left(\frac{L_* V_{\mathrm{exp}}\langle Q \rangle}{\dot{M}c}\right)^{1/2}, \quad (3)$$

where L_* is the stellar luminosity, V_{exp} is the expansion velocity, $\dot{M}$ is the mass-loss rate, c is the speed of light, and $\langle Q \rangle$ is the flux-averaged extinction coefficient of dust particles estimated in the previous section. The same dust to gas ratio of $\Psi = 5 \times 10^{-3}$ is used to calculate the heating rate.

Generally, in oxygen-rich envelopes the main coolants are H_2O and CO molecules. The contribution of H_2O molecules to the cooling process in IRC+10420 is quite uncertain. We note that far-IR emission lines of H_2O are not detected in the ISO data (Molster et al. 2002). In addition, OH masers are seen in a shell of radius $1''-1''.5$ (Nedoluha & Bowers 1992). Because OH
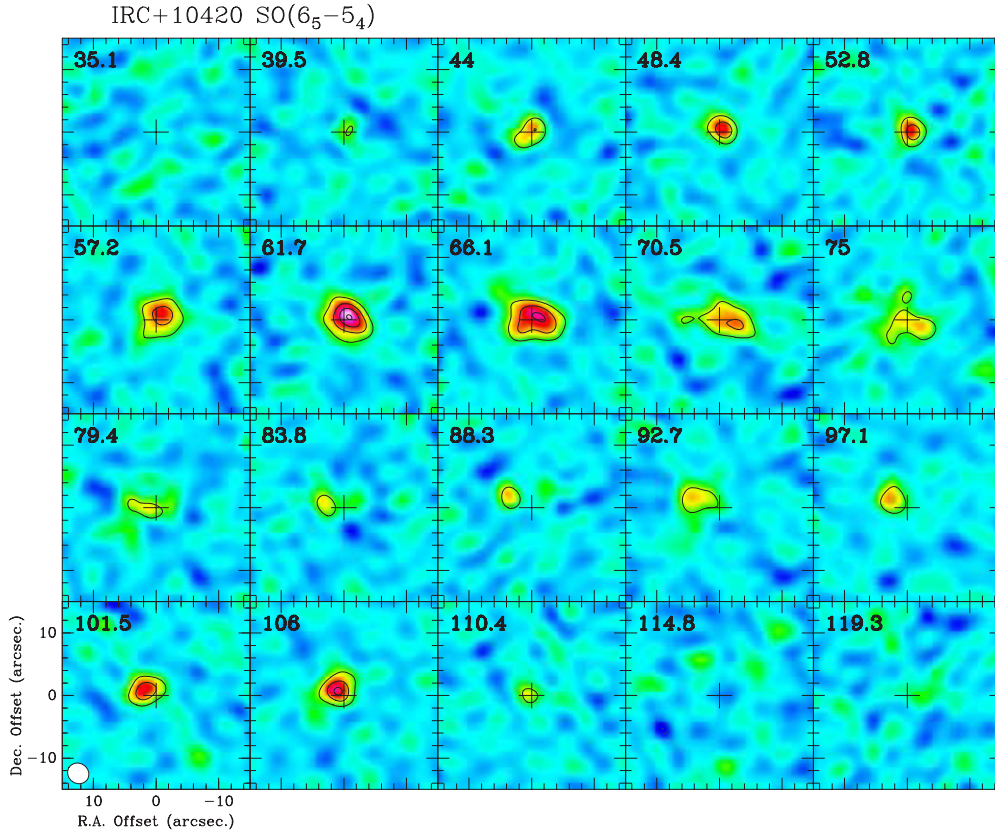
IRC+10420 SO(6_5–5_4)

Figure 6. Channel maps of the SO $J_K = 6_5$–5_4 line emission obtained from the SMA compact configuration alone. The synthesized beam is $3''.51 \times 3''.21$ (PA $= 63°$) and is indicated in the bottom left corner of the figure. Contour levels are drawn every 0.2 Jy beam^{-1} or 0.45 K ($\sim 4\sigma$). The velocity resolution is 4.4 km s^{-1}. The cross indicates the position of the continuum peak emission.

(A color version of this figure is available in the online journal.)

radical is the photodissociation product of H_2O, it is likely that H_2O molecules can only exist at even smaller radii, i.e., inside the central cavity discussed previously. Therefore, we do not expect the H_2O molecules to be present in significant quantity in the part of the molecular envelope traced in CO emission As a result, we do not include the cooling due to the H_2O molecule in our model and calculate the cooling solely due to CO molecule and its isotopomer ^{13}CO.

We use the thermal balance and radiative transfer model published by Dinh-V-Trung & Nguyen-Q-Rieu (2000) to derive the temperature profile of the molecular gas and to calculate the excitation of CO molecules and predict the strength of CO rotational transitions. We take into account all rotational levels of CO molecules up to $J = 20$. The collisional cross sections with H_2 are taken from Flower (2001), assuming an ortho to para ratio of 3 for molecular hydrogen. The local linewidth is determined by the turbulence velocity and the local thermal linewidth. Because the expansion velocity of the gas in the envelope of IRC+10420 is large and the observed CO line profiles have smooth slopes at both blueshifted and redshifted edges (see Figure 11), we need to assume a constant turbulence velocity of 3 km s^{-1}. We note that this is higher than normally used (about 1 km s^{-1}) for the envelope around AGB stars where the expansion velocity is lower (Justtanont et al. 1994). In our model, the spherical envelope is covered with a grid of 90 radial points. For each rotational transition, the radiative transfer equation is integrated accurately through the envelope to determine the average radiation field at each radial mesh point. We use the approximate lambda operator method together with Ng-acceleration to update the populations

of CO molecules of different energy levels. Once convergence is achieved, we convolve the predicted radial distribution of the line intensity with a Gaussian of specified FWHM to produce simulated data for comparison with observations.

As discussed in the previous section, there is a clear evidence for the presence of two molecular shells from our SMA data. The size and location of each molecular shell are determined from fits to the interferometric data. In our model, we adjust both the mass-loss rates and the relative abundance of CO molecules in the two molecular shells to match both the single dish and interferometric data. We find that a relatively low mass-loss rate similar to that derived by Castro-Carrizo et al. (2007) would result in a too high gas temperature in the envelope as the heating term becomes more dominant in comparison to the cooling term. We also find that a high abundance of CO of a few times 10^{-4} as usually used for oxygen-rich envelopes (Kemper et al. 2003; Castro-Carrizo et al. 2007) would result in CO lines that are too strong. Instead, a relative abundance of 10^{-4} for CO molecules with respect to H_2 provides reasonable fit to all the available data. The radial profile of the gas temperature is shown in Figure 10. The sudden jump in gas temperature at the inner radius of the second shell ($\sim 1.85 \times 10^{17}$ cm) is due to the change in the mass-loss rate. We can see that the gas temperature in the envelope of IRC+10420, although lower than assumed in Castro-Carrizo et al. (2007), is higher than that typically found in circumstellar envelopes. Even at the outermost radius of the envelope, the gas temperature is still around 50 K. For comparison, in the envelope around OH/IR stars, the gas temperature at similar radial distances from the central star is predicted to be much lower, 10 K or even less (Justtanont et al. 1994; Groenewegen
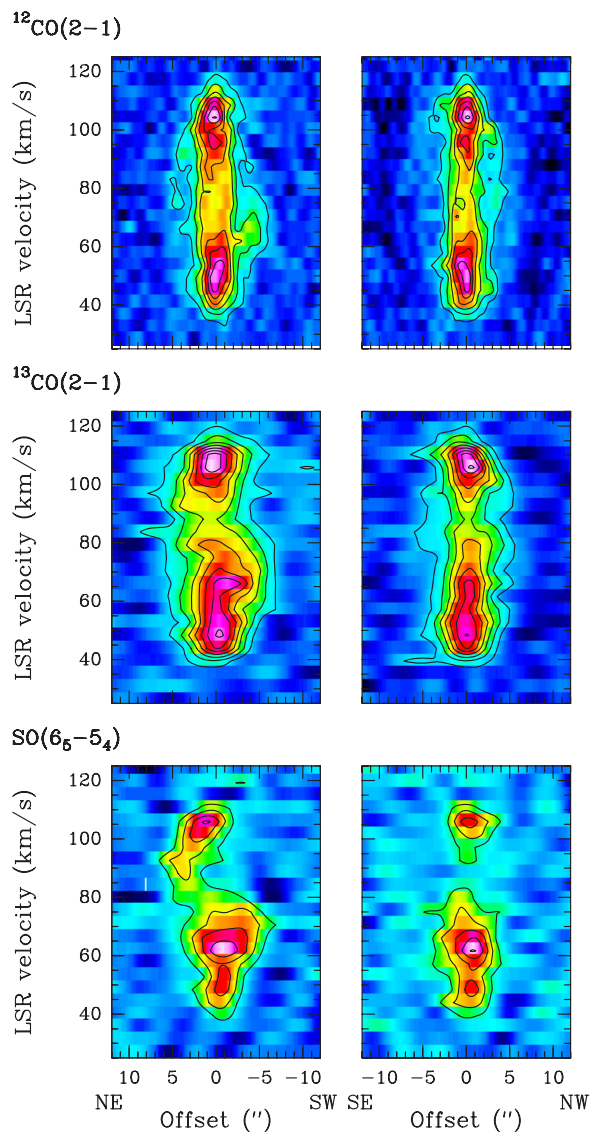
^{12}CO(2−1)

^{13}CO(2−1)

SO(6_5−5_4)

Figure 7. PV diagrams along the major axis, defined at PA = 70° (left) and perpendicularly along the minor axis (right). Contour levels are every 0.24 Jy beam^{-1} for ^{12}CO $J = 2$–1 and every 0.2 Jy beam^{-1} for ^{13}CO $J = 2$–1 and SO 6_5–5_4.

(A color version of this figure is available in the online journal.)
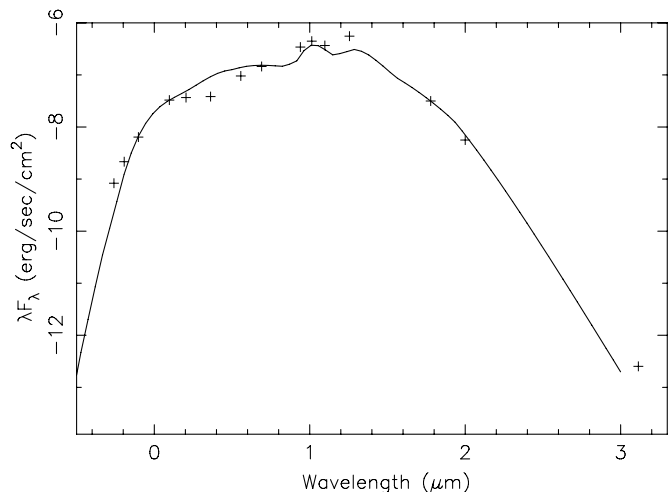
Figure 8. SED of IRC+10420. The crosses denote observational data from Jones et al. (1993) and Oudmaijer et al. (1996). The solid line represents the model SED.
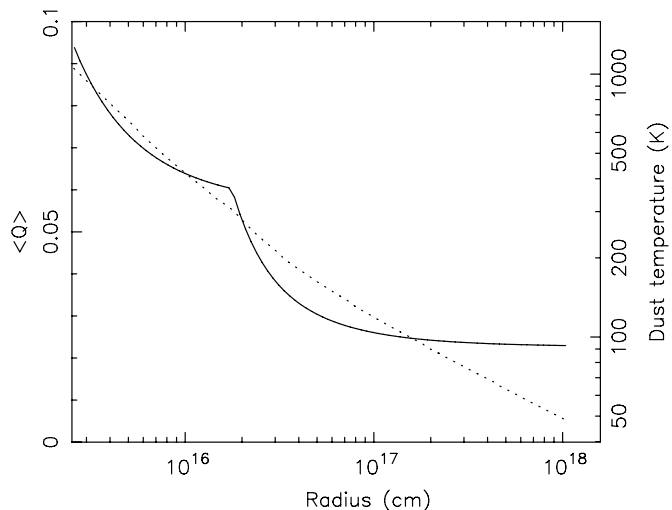
Figure 9. Dust temperature profile (dotted line) and flux-averaged extinction coefficient $\langle Q \rangle$ (solid line) in the envelope of IRC+10420 obtained from matching the model prediction of the SED to the observational data.
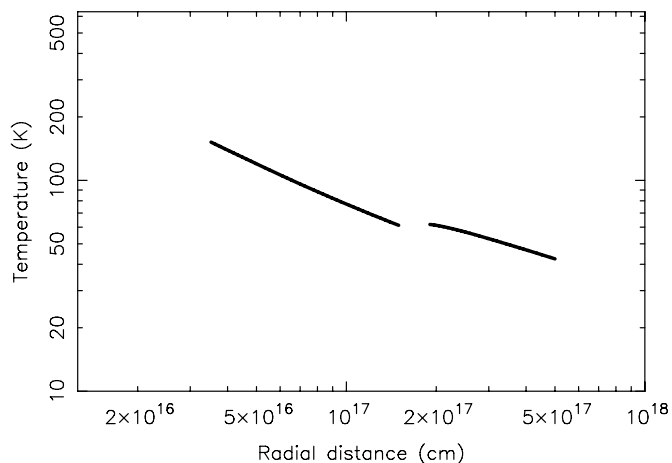

Figure 10. Predicted radial profile of the molecular gas temperature in the envelope of IRC+10420.

Table 3
Parameters of the Model for IRC+10420 Envelope

Parameters	Shell I	Shell II
Inner radius	3.5×10^{16} cm	1.85×10^{17} cm
Outer radius	1.5×10^{17} cm	5×10^{17} cm
Mass-loss rate, $\dot{M}$	$9 \times 10^{-4}\ M_\odot$ yr^{-1}	$7 \times 10^{-4}\ M_\odot$ yr^{-1}
Expansion velocity, $V_{\rm exp}$	38 km s^{-1}	38 km s^{-1}
Dust to gas ratio, Ψ	5×10^{-3}	5×10^{-3}
Momentum transfer coefficient, $\langle Q \rangle$	0.025	0.025
^{12}CO/H$_2$	10^{-4}	10^{-4}
^{13}CO/H$_2$	1.5×10^{-5}	1.5×10^{-5}
Turbulent velocity	3 km s^{-1}	3 km s^{-1}

1994). The main reason for the elevated gas temperature in the envelope of IRC+10420 is the strong heating due to the enormous luminosity of the central yellow hypergiant. The cooling due to molecular emissions is also affected by the lower abundance of CO, that we find necessary to match the data. A summary of the parameters used in our model is presented in Table 3.

As shown in Figures 11–14, the results of our model are in reasonable agreement with both the strengths of CO lines
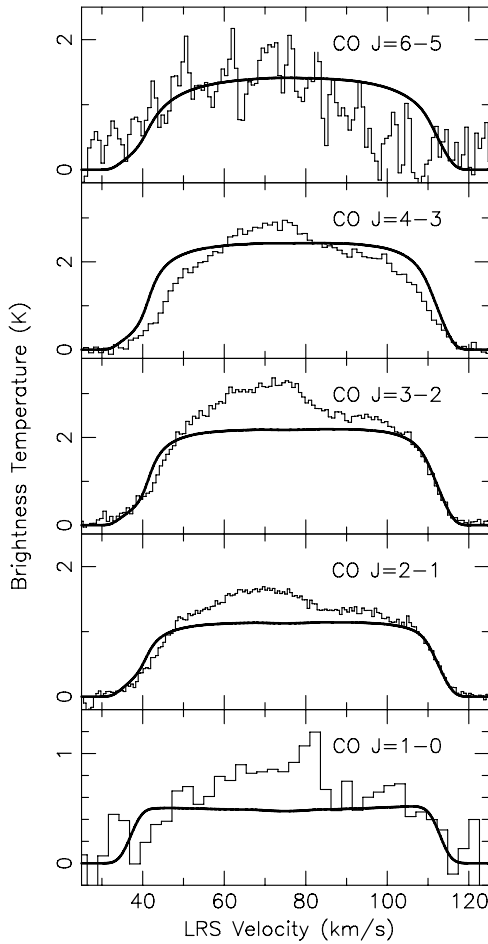
Figure 11. Comparison between observations of CO transitions from Kemper et al. (2003) and Teyssier et al. (2006) and our model predictions. The telescope beams are $22''$ for $J = 1$–0, $19''.7$ for $J = 2$–1, $13''.2$ for $J = 3$–2, $10''.8$ for $J = 4$–3, and $10''.3$ for $J = 6$–5 line, respectively.
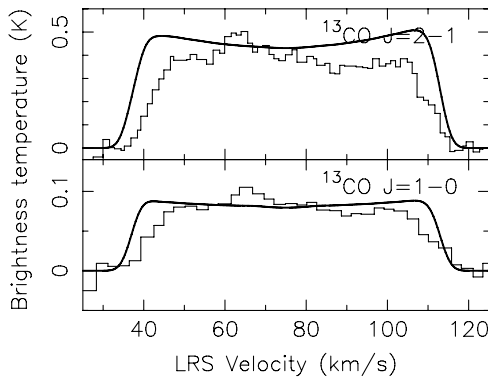

Figure 12. Comparison between the observed ^{13}CO $J = 1$–0 and $J = 2$–1 lines observed by Bujarrabal et al. (2001) and our model predictions (thick solid line). The telescope beams are $22''$ for $J = 1$–0 and $12''$ for $J = 2$–1 line, respectively.

measured by single dish telescopes and the radial distribution of brightness temperature of $J = 1$–0 and $J = 2$–1 lines observed with interferometers. We note that except for the extra emission in the blue part of the line profile between 65 and 75 km s^{-1}, the shape of the $J = 2$–1 and $J = 3$–2 is in close agreement with observation. Higher transitions $J = 4$–3 and 6–5 show some evidence of narrower linewidth than predicted by the
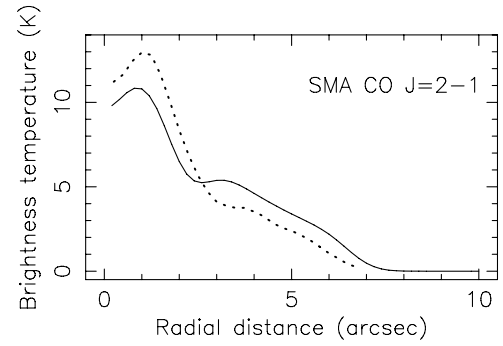

Figure 13. Azimuthal average of the ^{12}CO $J = 2$–1 brightness temperature (dotted line) obtained from SMA data at velocity channel $V_{\rm LSR} = 75$ km s^{-1}, and the model prediction (solid line).
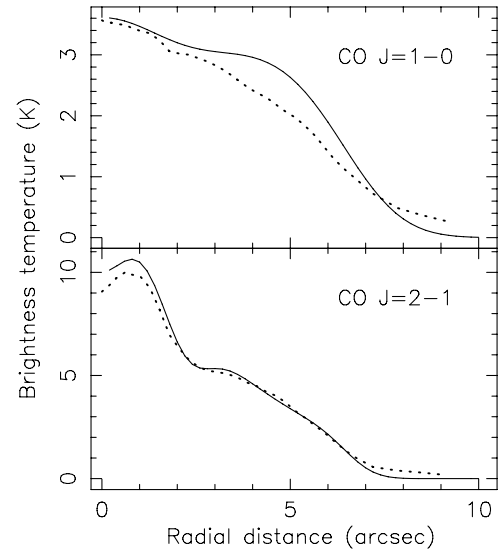

Figure 14. Comparison between the radial distribution of surface brightness (dotted line) of CO $J = 1$–0 and $J = 2$–1 observed with the Plateau de Bure interferometer (Castro-Carrizo et al. 2007) and our model predictions (solid line). The angular resolution is $2''.86$ for the CO $J = 1$–0 and $1''.4$ for the CO $J = 2$–1, respectively

model. One possible explanation is that the expansion velocity in the inner region traced by these high-lying transitions has slightly lower expansion velocity than in the outer part of the envelope.

By comparing the model predictions with the strengths of ^{13}CO $J = 1$–0 and $J = 2$–1 lines observed with the IRAM 30 m telescope (Bujarrabal et al. 2001), we derive a relative abundance for ^{13}CO/H$_2$ of 1.5×10^{-5}, or an isotopic ratio ^{12}C/^{13}C ~ 6. This ratio is very similar to the values ^{12}C/^{13}C $= 6$ and 12, respectively, found in the red supergiants α Ori and α Sco (Harris & Lambert 1984; Hinkle et al. 1976). Such a low isotopic ratio suggests that IRC+10420 has experienced a significant mixing of H burning products to its surface prior to the ejection of the material in the envelope.

The difference between the mass-loss rates and gas temperature profile derived from our modeling and that obtained by Castro-Carrizo et al. (2007) can be understood as the consequence of the higher gas temperature and higher CO abundance adopted in their work. For the same strength of the CO rotational lines, the higher CO abundance can be almost exactly compensated by a corresponding decrease in the mass-loss rate.

Our results indicate the presence of two separate shells (shell I and shell II, see Table 3) with slightly different mass-loss rates.

With an expansion velocity of 38 km s^{-1}, the time interval between the two shells is $\sim$200 yr. The cavity inside shell I also implies a dramatic decrease in mass loss from IRC+10420 over the last $\sim$300 yr. Thus, IRC+10420 loses mass in intense bursts, separated by relatively quiet periods of a few hundreds years in duration.

4.3. Caveats

In our model, we consider separately the dust and gas component in the envelope of IRC+10420. The dust continuum emission model is used as a simple way to estimate the $\langle Q \rangle$ parameter of dust particles, which is needed for the thermal balance calculation in the molecular shells. It turned out that the mass-loss rates of the molecular shells between 9×10^{-4} $M_\odot$ yr^{-1} for shell I and 7×10^{-4} $M_\odot$ yr^{-1} for shell II are lower but quite close to the mass-loss rate of 1.2×10^{-3} $M_\odot$ yr^{-1} of the cool outer dust shell inferred from the modeling the SED of the envelope. Our approach, although less ad hoc than simply assuming a value of the $\langle Q \rangle$ parameter for dust particles, is not fully self-consistent in the treatment of the dust and gas component. It would be desirable in the future to treat both the dust and gas component together when high angular resolution data on the dust continuum emission and higher J lines of CO become available.

Another caveat of our model is the assumption that the heating of molecular gas is mainly due to collision between dust particles and gas molecules. The high luminosity of the central star of IRC+10420 suggests that radiation pressure on dust particles is a possible mechanism for driving the wind as assumed in our mode. However, given the high expansion velocity and the presence of many small scale features in high angular resolution optical images of the envelope (Humphreys et al. 1997), which has been interpreted as jets or condensations, other mechanisms such as shocks produced by interaction between higher velocity ejecta and the envelope should be considered. The heating due shocks within the envelope might contribute to the thermal balance of the molecular gas in IRC+10420.

5. COMPARISON WITH OPTICAL IMAGING DATA

The circumstellar envelope around IRC+10420 is known to be very complex, with a number of peculiar structures (Humphreys et al. 1997). In the outer part of the envelope at radial distance of $\sim$3$''$–6$''$, several arclike features can be seen. These features have been interpreted as representing different mass-loss episodes of IRC+10420. In addition, condensations or blobs are seen closer (about 1$''$–2$''$ in radius) to the central star. That might represent a more recent mass-loss episode. These features correspond spatially to the two molecular shells (shell I and II) identified in our observations. In addition, Humphreys et al. (1997) also identified several broad fan-shaped features to the southwest side of the central star, between radius of 0$\farcs$5 and 2$''$. From their higher surface brightness in comparison with other parts of the envelope, Humphreys et al. (1997) suggest that these features are ejecta moving obliquely toward the observer. As discussed in the previous section, the channel maps of ^{13}CO $J = 2$–1 and SO $J_{\rm K} = 6_5$–5$_4$ (Figures 5 and 6) reveal enhanced emissions in blueshifted velocity channels together with a positional shift of the emission centroid also to the southwest quadrant of the envelope. Therefore, the spatial kinematics obtained from our observations and the properties of these fan-shaped features are consistent with the presence of an ejecta in the southwest side of the envelope around IRC+10420.

6. SUMMARY

We have used the SMA to image and study the structure of the molecular envelope around IRC+10420. Our observations reveal a large expanding envelope with a clumpy and very complex structure. The envelope shows clear asymmetry in ^{12}CO $J = 2$–1 emission in the southwest direction at position angle PA $\sim$ 70°. The elongation of the envelope is found even more pronounced in the emission of ^{13}CO $J = 2$–1 and SO $J_{\rm K} = 6_5$–5$_4$. A positional shift with velocity is seen in the above emission lines, suggesting the presence of a weak bipolar outflow in the envelope of IRC+10420.

In the higher resolution data of ^{12}CO $J = 2$–1, we find that the envelope has two components: (1) an inner shell (shell I) located between radius of about 1$''$ and 2$''$; (2) an outer shell (shell II) between radius 3$''$ and 6$''$. These shells represent two previous mass-loss episodes from IRC+10420.

We constrain the physical conditions inside the envelope by modeling the dust properties, the heating and cooling of molecular gas. From comparison with observations we derive the size and the location of each molecular shell. We estimate a mass-loss rate of $\sim$9$\times10^{-4}$ $M_\odot$ yr^{-1} for shell I and 7×10^{-4} $M_\odot$ yr^{-1} for shell II. The gas temperature is found to be usually high in IRC+10420 in comparison with other oxygen-rich envelopes, mainly due to the large heating induced by the large luminosity of the central star.

We also derive a low isotopic ratio ^{12}C/^{13}C $= 6$ for IRC+10420, which suggests a strong mixing of processed material from stellar interior to the surface of the star.

REFERENCES

Blöcker, T., Balega, Y., Hofman, K. H., Lichtenthaler, J., Osterbart, R., & Weigelt, G. 1999, A&A, 348, 805
Bujarrabal, V., Castro-Carrizo, A., Alcolea, J., & Sánchez-Contreras, C. 2001, A&A, 377, 868
Castro-Carrizo, A., Lucas, R., Bujarrabal, V., Colomer, F., & Alcolea, J. 2001, A&A, 368, L34
Castro-Carrizo, A., Quintana-Lacaci, G., Bujarrabal, V., Neri, R., & Alcolea, J. 2007, A&A, 465, 457
Davies, B., Oudmaijer, R. D., & Sahu, K. C. 2007, ApJ, 671, 2059
de Jager, C. 1998, A&AR, 8, 145
Dinh-V-Trung & Nguyen-Q-Rieu 2000, A&A, 361, 601
Flower, D. R. 2001, J. Phys. B, 34, 2731
Goldreich, P., & Scoville, N. 1976, ApJ, 205, 144
Groenewegen, M. 1994, A&A, 290, 544
Harris, M. J., & Lambert, D. L. 1984, ApJ, 281, 739
Hinkle, K. H., Lambert, D. L., & Snell, R. L. 1976, ApJ, 210, 684
Humphreys, R. M., Smith, N., Davidson, K., Jones, T. J., Gehrz, D., & Mason, C. 1997, AJ, 114, 2778
Humphreys, R. M., Strecker, D. W., Murdock, T. L., & Low, F. J. 1973, ApJ, 179, L49
Jones, T. J., et al. 1993, ApJ, 411, 323
Justtanont, K., Skinner, C. J., & Tielens, A. G. G. M. 1994, ApJ, 435, 852
Kemper, F., Stark, R., Justtanont, K., de Koter, A., Tielens, A. G. G. M., Waters, L. B. F. M., Cami, J., & Dijkstra, C. 2003, A&A, 407, 609
Klochkova, V. G., Chentsov, E. L., & Panchuk, V. E. 1997, MNRAS, 292, 19
Knapp, G. R., & Morris, M. 1985, ApJ, 292, 640

Menten, K. M., & Alcolea, J. 1995, ApJ, 448, 416
Molster, F. J., Waters, L. B. F. M., Tielens, A. G. G. M., & Barlow, M. J. 2002, A&A, 382, 184
Muller, S., Dinh-V-Trung Lim, J., Hirano, N., Muthu, C., & Kwok, S. 2007, ApJ, 656, 1109
Nedoluha, G. E., & Bowers, P. F. 1992, ApJ, 392, 249
Omont, A., Lucas, R., Morris, M., & Guilloteau, S. 1993, A&A, 267, 490
Oudmaijer, R. D. 1998, A&AS, 129, 541
Oudmaijer, R. D., Groenewegen, M. A. T., Matthews, H. E., Blommaert, J. A. D. L., & Sahu, K. C. 1996, MNRAS, 280, 1062

Quintana-Lacaci, G., Bujarrabal, V., Castro-Carrizo, A., & Alcolea, J. 2007, A&A, 471, 551
Sahai, R., & Wannier, P. G. 1992, ApJ, 394, 320
Sánchez-Contreras, C., Bujarrabal, V., Neri, R., & Alcolea, J. 2000, A&A, 357, 651
Teyssier, D., Hernandez, R., Bujarrabal, V., Yoshida, H., & Phillips, T. G. 2006, A&A, 450, 167
Volk, K., & Kwok, S. 1988, ApJ, 331, 435
Walsmley, C. M., Chini, R., Kreysa, E., Steppe, H., Forveille, T., & Omont, A. 1991, A&A, 248, 555
Willacy, K., & Millar, T. J. 1997, A&A, 324, 237